

A&A manuscript no.
(will be inserted by hand later)

Your thesaurus codes are:
11 (11.01.1; 11.05.1; 11.05.2; 11.09.4; 09.16.1)

ASTRONOMY
AND
ASTROPHYSICS

Planetary nebulae in M32 and the bulge of M31: Line intensities and oxygen abundances

Michael G. Richer¹ *, **, Grażyna Stasińska² **, and Marshall L. McCall³

¹ Instituto de Astronomía, UNAM, Apartado Postal 70-264, 04510 México, D. F., México
email: richer@astroscu.unam.mx

² DAEC, Observatoire de Meudon, 5 Place Jules Janssen, F-92195 Meudon Cedex, France
email: grazyna@obspm.fr

³ Dept. of Physics and Astronomy, York University, 4700 Keele Street, Toronto, Ontario, Canada M3J 1P3
email: mccall@aries.phys.yorku.ca

Received ? / Accepted ?

Abstract. We present spectroscopy of planetary nebulae in M32 and in the bulge of M31 that we obtained with the MOS spectrograph at the Canada-France-Hawaii Telescope. Our sample includes 30 planetary nebulae in M31 and 9 planetary nebulae in M32. We also observed one H II region in the disk of M31. We detected [O III] $\lambda 4363$ in 18 of the planetary nebulae, 4 in M32 and 14 in the bulge of M31. We use our line intensities to derive electron temperatures and oxygen abundances for the planetary nebulae.

Key words: planetary nebulae – M31 – M32 – oxygen abundances

1. Introduction

One of the most important clues concerning the early evolution of dynamically hot galaxies (DHGs: ellipticals, dwarf spheroidals, and bulges of spirals) in the fundamental plane of galaxies is the existence of a well-defined relationship between metallicity and mass (e.g., Bender et al. 1993). The fundamental lesson taught by this relation is that star formation in DHGs stopped because of gas loss, with less massive systems losing greater fractions of their gas. Outflow probably begins when supernovae have raised the internal energy of the gas enough to allow it to escape the potential well (e.g., Brocato et al. 1990).

Most commonly, the metallicity in DHGs is measured via the Mg_2 index. While the Mg_2 index is an excellent means of ranking galaxy metallicities, it does not yield

an abundance directly, i.e., the number density of a particular element relative to hydrogen, and calibrations of the Mg_2 index (model-dependent) are usually in terms of the iron abundance, an element whose production is notoriously difficult to model. Though this may be best for some purposes, e.g., studies of stellar populations, it is not sufficient for all purposes. To study the chemical evolution of DHGs requires the abundance of an element whose production is well understood. Were such abundances available, there would be some hope of quantifying the gas fraction at which DHGs of different masses begin to lose mass. Knowledge of the abundances would admit studying the yield of heavy elements, and hence the slope of the stellar initial mass function during the star formation epoch. Given the known photometric and dynamical properties of DHGs today, abundances would also allow us to study the global energetics involved during their star formation phase.

This paper is one of a sequence investigating the oxygen abundances of DHGs. Here, we present oxygen abundances for samples of planetary nebulae in M32 and in the bulge of M31. These two nearby systems are good representatives of typical DHGs. Though M32's light profile may be truncated compared to isolated ellipticals, its structural, dynamical, and spectral properties are perfectly typical for an elliptical of its luminosity (Kormendy 1985; Bender et al. 1993). Similarly, recent work on the DHG fundamental plane has shown that the photometric, dynamical, and stellar population properties of bulges follow those of pure ellipticals (Bender et al. 1992, 1993).

Oxygen is an excellent element with which to study the evolution of galaxies. Oxygen is a primary element whose sole significant production site is type II supernovae (Wheeler et al. 1989), so its abundance is tied directly to the history of massive star formation, and the enrichment time scale is short compared to the gas consumption time scale. Oxygen abundances are also easily observable in planetary nebulae. Planetary nebulae have

Send offprint requests to: M. G. Richer

* The overwhelming majority of my work on this project was done while I was at the Observatoire de Meudon as a member of the DAEC.

** Visiting Astronomer, Canada-France-Hawaii Telescope, operated by the National Research Council of Canada, the Centre National de la Recherche Scientifique de France, and the University of Hawaii

Table 1. Observing Log

Date	Object	Grism	Dispersion	Spectral Range ^a	Exposures	Standards
1994 Aug 1/2	M32	U900	0.9Å/pixel	3727Å-H γ	1 \times 2700s	Feige 15
1994 Aug 2/3	NGC 6720	U900	0.9Å/pixel	3600Å-5400Å	3 \times 1500s	Feige 15
					1 \times 1200s	
	M32	U900	0.9Å/pixel	3727Å-H γ	3 \times 2700s	Feige 15
	M32	O300	3.5Å/pixel	4686Å-1 μ m	1 \times 900s	Wolf 1346
					1 \times 1800s	
1994 Aug 3/4	M32	B600	1.5Å/pixel	3727Å-5876Å	1 \times 1800s	Wolf 1346
						Feige 15
	M31	B600	1.5Å/pixel	3727Å-5876Å	3 \times 2700s	Wolf 1346
					1 \times 1200s	Feige 15

^a These are *minimum* spectral ranges. The actual spectral range will depend upon the object's position within the spectrograph's field of view.

high electron temperatures, so the temperature-sensitive [O III] λ 4363 line is observable, making it possible to determine accurate electron temperatures in high metallicity environments. Further, the dominant ionization stages of oxygen, O⁺ and O⁺⁺, have observable lines, while other ionization stages are easily accounted for using ratios of readily detectable helium lines (e.g., Kingsburgh & Barlow 1994).

Planetary nebulae are good sites in which to probe the oxygen abundance, and they are the only sites that are directly accessible in DHGs. Since planetary nebulae are bright in strong emission lines (e.g., [O III] λ 5007), they are easily located within their parent galaxies using emission-line and continuum-band imaging (e.g., Ciardullo et al. 1989). Observational and theoretical evidence indicates that the stellar precursors of most planetary nebulae do not modify their initial oxygen abundance (Iben & Renzini 1983; Henry 1989; Perinotto 1991; Forestini & Charbonnel 1997). Hence, a planetary nebula's oxygen abundance reflects that in the interstellar medium at the time of its precursor's formation. Finally, most of the stellar populations in DHGs are old, so they will produce planetary nebulae at comparable rates per unit mass. As a result, planetary nebulae sample the oxygen abundances in DHGs according to the mass in each stellar population. The resulting mean oxygen abundance for the planetary nebula population in a DHG should then be a mass-weighted mean of the oxygen abundances in its stellar populations.

Apart from their utility for studying the chemical evolution of M31 and M32, the spectroscopic data for the planetary nebulae we present are interesting for what they reveal about the evolution of the planetary nebulae themselves. Though there may exist a good qualitative understanding of planetary nebula evolution, it is unclear how well it stands up to quantitative scrutiny. This situation arises primarily because the distances to planetary nebulae are difficult to establish within the Milky Way. Traditionally, this constraint has made it difficult to study such

absolute properties as the luminosity and size of planetary nebulae, as well as the temporal evolution of these quantities. Extragalactic planetary nebulae are especially valuable in this regard because their distances are known. The addition of the data sets for M32 and the bulge of M31 is particularly helpful since these planetary nebulae arise from old stellar populations. They will thus provide an intriguing contrast with the planetary nebula populations in the Magellanic Clouds, which are the product of recent star formation (Richer 1993). Whether the evolution of planetary nebulae depends upon the progenitor mass or metallicity are among the questions that we may hope to answer through a comparison of the properties of planetary nebulae in M31 and M32 with those elsewhere. A better quantitative understanding of planetary nebula evolution would be a great help in understanding and using the planetary nebula luminosity function as a distance indicator.

In this paper, we present our spectroscopic data for our samples of planetary nebulae in M32 and in the bulge of M31. The observations and their reductions are described in Section 2. The line intensities and reddenings we deduce are presented in Section 3. The reddening-corrected line intensities are then used to calculate electron temperatures and oxygen abundances in Section 4. Summary comments are given in Section 5.

In companion papers, we will use the data we present below to study the chemical evolution of DHGs and the evolution of planetary nebulae in different environments.

2. Observations and reductions

Our ultimate purpose for making these observations was to study the chemical evolution of M32 and the bulge of M31. In M31, we chose planetary nebulae in the inner bulge in order to probe the highest levels of enrichment. On account of the bright galaxy background, we also preferentially chose planetary nebulae that were known to be

Table 2. B600/O300 Sensitivity Correction

Wavelength	I(B600)/I(O300)	M32 Planetary Nebulae Used ^a
H β	1.17 ± 0.06	all, except PN25
[O III] λ 4959	1.00 ± 0.01	PN1, PN2, PN4, PN5, PN7, PN8, PN17, PN24
He I λ 5876	0.77 ± 0.03	PN1, PN7, PN8, PN11, PN17
H α	0.85 ± 0.02	PN2, PN8, PN11, PN17, PN24

^a PN4 and PN17 are background objects in the disk of M31 (Ford & Jenner 1975).

bright in [O III] λ 5007. All of the objects we observed in M31 are found within the inner half effective radius of M31’s bulge. In M32, we observed as many objects as we could, again emphasizing bright objects on account of the galaxy background. In this case, the objects we observed extended to many effective radii.

We obtained our observations over three nights in August 1994 at the Canada-France-Hawaii Telescope (CFHT) with the multi-object spectrograph (MOS). The MOS is an imaging, multi-slit spectrograph that employs a grism as the dispersing element (see Le Fèvre et al. 1994 for details). Objects are selected for spectroscopy using focal plane masks that are constructed on-line from previously acquired images. The detector was the Loral3 CCD, a thick CCD with $15\mu\text{m}$ square pixels in a 2048×2048 format, coated to enhance the quantum efficiency in the blue. The Loral3’s read noise was 8 electrons and its gain was set to 1.9 electrons/ADU. For the observations of both M31 and M32, we used slits $15''$ long by $1''$ wide. No order-sorting filter was used for any of these observations.

Table 1 presents a log of our observations. During the course of the observations, we used three different grism set-ups in order to optimize throughput, wavelength coverage, and spectral resolution. We used the B600 grism only because of the disappointing throughput of the U900 grism. Although the precise dispersion and wavelength coverage depend upon each object’s position within the field of view, Table 1 lists typical values for all three grisms (minimal ranges for the wavelength coverage).

We used the standard IRAF routines to reduce the data (noao.imred.ccdred), and followed the standard reduction procedure. First, the overscan bias was removed from all of the images. Next, for the first two nights, sequences of zero exposure images were combined and subtracted from the other images to remove any bias pattern. This was not done on the third night because the CCD dewar began to warm up before we had a chance to obtain the zero exposure images. This is unlikely to be a limitation, since no bias pattern was obvious on either of the first two nights. Finally, pixel-to-pixel variations were removed using spectra of the internal quartz lamp.

Extracting the spectra proved challenging on account of the nature and faintness of the sources, and on account of the characteristics of the spectrograph. The planetary

nebulae in M31 and M32 are sufficiently faint that we were unable to detect their continuum emission. Only the emission lines were visible, appearing as a sequence of dots, so it was impossible to trace these spectra. Furthermore, the spectra spanned the full width of the detector, so they suffered from geometric distortion (pin-cushion) introduced by the optics of the spectrograph. Fortunately, we had to include star apertures when defining the spectrograph’s focal plane mask to permit accurate re-alignment on the field when ready to do spectroscopy. We used these stars (6 for M31, 3 for M32) to map the geometric distortion imposed by the optics, and corrected this distortion using the tasks in the noao.twodspec.longslit package (Anderson 1987). At this point, we had images in which the wavelength axis was parallel to the rows of the CCD, and we could use the brightest line in each spectrum to define an extraction aperture (e.g., Massey et al. 1992). Except for the U900 spectra, the individual spectra were extracted from each image and then combined to produce the final combined spectra. To better define the extraction apertures for the U900 spectra, the spectra were combined first, after verifying that the individual images had the same spatial coordinate scales. In all cases, extraction involved local subtraction of the underlying galaxy and sky spectra.

Establishing a consistent sensitivity scale across all three grism set-ups was a primary consideration of our data reduction. We calibrated the instrumental sensitivity for each set-up using observations of the spectrophotometric standard stars listed in Table 1. We verified that our slitlet-to-slitlet sensitivity scale was secure in three ways. First, the observations of the standard stars were made in pairs through two different slitlets. These slitlets were cut at the red and blue extremes of the field of view to ensure that our standard star observations spanned the full wavelength range of our planetary nebula observations. These paired observations of the standard stars had 500Å, 800Å, and 1900Å of spectrum in common for the U900, B600, and O300 grisms, respectively. In these overlap regions, the sensitivity functions for each grism (on each night) were in agreement. Second, we obtained a spectroscopic sky flat through the standard star mask with the B600 grism on the last night. This mask contained two slitlets in addition to those used for the standard star

observations. Comparing the night sky spectra through these four slitlets indicates that variations in the wavelength sensitivity between different slitlets are less than 4.5% (rms). Finally, observations of NGC 6720 were obtained through a different mask than the standard stars, and no wavelength-dependent trends are seen in its sensitivity calibration (see Table 3 below). Therefore, though we did not observe the standard stars through the slitlets used for our program objects, we have no reason to believe that our sensitivity calibration is slitlet-dependent.

We then chose the O300 observations of the planetary nebulae in M32 as our reference data set. This choice was motivated by a number of considerations. First, these planetary nebulae were observed with all three grisms. Second, the O300 grism has good sensitivity over the $H\beta$ – $H\alpha$ wavelength range (Le Fèvre et al. 1994), which contains the strongest lines in the spectra. Third, our reddening values for these planetary nebulae (see Tables 6, 7, and 8) were reasonable, typically $E(B - V) < 0.2$ mag, and invariably positive. These reddenings were consistent with previous observations of PN1 in M32 (Ford et al. 1978). The reddening towards M32 is also expected to be small if it is in front of the disk of M31 (e.g., Burstein & Heiles 1984).

We ensured that there were no systematic differences between the B600 and O300 data sets by comparing the intensities of $H\beta$, $H\alpha$, $[O\text{ III}]\lambda 4959$, and $\text{He I } \lambda 5876$ measured relative to $[O\text{ III}]\lambda 5007$ for the planetary nebulae in M32. In making these comparisons, we considered only those objects for which we had the best detections of these lines. For these objects, we computed the ratio of the line intensity in the B600 spectrum to that in the O300 spectrum. Table 2 lists the mean value of this ratio, the standard error in the mean, and the objects we considered for each line. Clearly, the main wavelength-dependent trend in Table 2 is a systematic decrease in the B600 sensitivity relative to the O300 sensitivity as one goes to longer wavelengths. Simply fitting a line to the values in Table 2 as a function of wavelength, however, yields a rather poor correction at $H\alpha$. As a result, for wavelengths between any two lines found in Table 2, we corrected for the difference in sensitivity calibrations by interpolating linearly between the corrections in Table 2. For lines to the blue of $H\beta$ or to the red of $H\alpha$, we adopted the $H\beta$ or $H\alpha$ corrections, respectively. We wondered if the upturn at $H\alpha$ in Table 2 could be due to second order contamination, but this seems unlikely. Both the O300 and B600 grisms have very low efficiency at 3250Å, and a second order contamination would affect the sensitivity calibration for both grisms similarly. Consequently, the upturn at $H\alpha$ appears to be real. The corrections in Table 2 were applied to the spectra of the planetary nebulae in both M32 and the bulge of M31.

The U900 data required no correction to put them on the O300 sensitivity scale. We deduced this from direct comparison with the B600 and O300 data (Tables 6, 7,

Table 3. Hydrogen Line Intensities for NGC 6720

	Line	Intensity ^a	$E(B - V)^a$
Aperture 1	$H\beta$	100.00 ± 1.49	
	$H\gamma$	42.07 ± 0.55	0.287 ± 0.034
	$H\delta$	24.03 ± 0.33	0.133 ± 0.023
	$H\epsilon$	12.99 ± 0.87	0.279 ± 0.093
	H8	7.14 ± 0.35	0.484 ± 0.061
	H9	5.79 ± 0.13	0.280 ± 0.027
	H10	3.97 ± 0.13	0.331 ± 0.037
	H11	2.85 ± 0.16	0.371 ± 0.060
	H12	2.32 ± 0.15	0.304 ± 0.070
Aperture 2	$H\beta$	100.00 ± 1.53	
	$H\gamma$	42.29 ± 0.57	0.273 ± 0.035
	$H\delta$	24.06 ± 0.34	0.131 ± 0.024
	$H\epsilon$	13.13 ± 0.90	0.264 ± 0.094
	H8	7.24 ± 0.36	0.467 ± 0.063
	H9	5.59 ± 0.19	0.320 ± 0.041
	H10	3.89 ± 0.15	0.355 ± 0.043
	H11	2.84 ± 0.19	0.375 ± 0.073
	H12	2.19 ± 0.18	0.366 ± 0.089
Aperture 3	$H\beta$	100.00 ± 1.45	
	$H\gamma$	42.51 ± 0.56	0.259 ± 0.035
	$H\delta$	24.72 ± 0.37	0.085 ± 0.025
	$H\epsilon$	13.11 ± 0.84	0.265 ± 0.088
	H8	7.91 ± 0.43	0.355 ± 0.068
	H9	5.58 ± 0.26	0.323 ± 0.056
	H10	3.77 ± 0.22	0.391 ± 0.064
	H11	3.15 ± 0.37	0.262 ± 0.129
	H12	2.60 ± 0.37	0.184 ± 0.151

^a The derivation of the uncertainties in the line intensities and reddening is described in Sec. 3.

and 8), and independently using a spectrum we obtained of the Galactic planetary nebula NGC 6720. Table 3 lists the intensities and reddening values for hydrogen lines in three regions of NGC 6720. The reddening values we derive from $H\gamma$, $H\epsilon$, H9, H10, H11, and H12 are in very good agreement in all three apertures, indicating that our U900 sensitivity calibration is good to 3750Å. Our reddening values at $H\delta$ are consistently 0.16 mag lower than calculated from $H\gamma$, so our U900 sensitivities may be underestimated by 15% near 4100Å. Our H8 reddening values are consistently high, but H8 was blended with $\text{He I } \lambda 3889$. We corrected the blend for the $\text{He I } \lambda 3889$ contribution using the $\text{He I } \lambda 4471$ intensity assuming no radiative transfer correction, thereby removing the maximum possible $\text{He I } \lambda 3889$ contribution (e.g., Aller 1987). Thus, it is perhaps not surprising that our H8 reddenings are too high. Overall, our Balmer line intensities for NGC 6720 indicate that our U900 sensitivity calibration is secure from 3750Å to $H\beta$. Similarly, for the planetary nebulae in M32 (Tables 6, 7, and 8), the U900 line intensities for $[O\text{ II}]\lambda 3727$, $[\text{Ne III}]\lambda 3869$, and $\text{He II } \lambda 4686$ are in excellent agreement with their B600 and O300 counterparts.

Figures 1 through 6 display the O300, B600, and U900 spectra of the planetary nebulae in M32, while Figures 7 through 12 display the B600 spectra of the planetary nebulae in the bulge of M31. The object designations (Ciardullo et al. 1989) are shown next to the spectra. Normally, the spectra are scaled such that H β occupies the full intensity scale, so stronger lines from adjacent spectra overlap, but some of the U900 and B600 spectra are scaled such that H γ and H α , respectively, occupy the full intensity scale. This scaling allowed the best compromise in demonstrating the signal-to-noise for various lines and an assessment of the background sky and galaxy subtraction. The full wavelength range is shown for the B600 and U900 spectra, but only the wavelength range below 7350Å is shown for the O300 spectra. Cosmic rays were not removed unless they interfered with the measurement of line intensities, and many remain in the spectra displayed in Figures 1 through 12.

3. Line intensities and reddening

Tables 6 to 9 (at end) list the adopted reddening-corrected line intensity ratios and reddening values for the planetary nebulae in M32 and the bulge of M31. We use the object designations from Ciardullo et al. (1989). The line intensities were measured using the software described by McCall et al. (1985). The uncertainties quoted for the line ratios are 1σ uncertainties that incorporate the uncertainties in both the line and H β fluxes. The uncertainties in the line fluxes include contributions from the fit to the line itself and from the noise in the continuum. In those instances where there is no line intensity value, but there is a line intensity uncertainty, e.g., He II $\lambda 4686$ in PN5 in M32, the “uncertainty” is a 2σ upper limit to the strength of undetected lines, and is based upon the noise observed in the continuum. Note that PN4 and PN17 in the M32 field have radial velocities indicating that they belong to the background disk of M31 (Ford & Jenner 1975). The H II region in the background disk of M31 that we observed in the M32 field is that denoted H II 1 by Ford & Jenner (1975).

For the planetary nebulae in M32, Tables 6 to 8 list the reddening-corrected O300, B600, and U900 line intensities, in addition to our adopted line intensities. The adopted intensities are those listed under the object name. Generally, we adopted the U900 line intensities in the blue and the O300 line intensities in the red, with the dividing line being He II $\lambda 4686$. He II $\lambda 4686$ is the only common exception to this rule. For He II $\lambda 4686$, we normally chose the line intensity from the spectrum in which the line was measured with the lowest relative error.

The reddening-corrected line intensities in Tables 6 through 9 are related to those we observed via

$$\log \frac{I(\lambda)}{I(\text{H}\beta)} = \log \frac{F(\lambda)}{F(\text{H}\beta)} - 0.4E(B-V)(A(\lambda) - A(\text{H}\beta))$$

where $F(\lambda)$ and $I(\lambda)$ are the observed and reddening-corrected line intensities, respectively, $E(B-V)$ is the reddening, and $A(\lambda)$ is the extinction for $E(B-V) = 1.0$ mag from the reddening law of Schild (1977). All of the line intensities for the planetary nebulae in M32 in Tables 6, 7, and 8 have been corrected for reddening using $E(B-V)$ determined from the O300 H α /H β ratio. For the U900 spectra that did not extend to H β , we corrected intensities relative to H γ using the O300 reddening, then adopted $I(\text{H}\gamma)/I(\text{H}\beta) = 0.47$. For the planetary nebulae in the bulge of M31, we determined the reddening from the H α /H β ratio in the two cases when it was available, but used the reddening calculated from the H γ /H β ratio otherwise. In all cases, we assumed intrinsic ratios of $I(\text{H}\alpha)/I(\text{H}\beta) = 2.85$ and $I(\text{H}\gamma)/I(\text{H}\beta) = 0.47$, which are appropriate for an electron temperature of 10^4 K and an electron density of 10^4 cm^{-3} (Osterbrock 1989). The reddening uncertainties reflect the 1σ uncertainties in the H α or H γ line intensities.

Note that the line intensities for PN408 in M31 are not corrected for reddening. For this faint object, we did not detect H γ , and H α fell outside our spectral window.

Since our reddenings are based upon different line intensity ratios for different objects, we consider them in greater detail before proceeding. All of our H α -based reddenings in Tables 6 through 9 are positive. The overwhelming majority of our H γ -based reddenings in Table 9 are also either positive or consistent with no reddening, but our 1σ H γ line intensity uncertainties do allow negative reddenings in four cases (PN3, PN43, PN48, and PN53). We considered not using H γ to determine the reddening, but rejected this option for four reasons. First, for the four planetary nebulae in M32 for which we measured an H γ intensity from the B600 spectrum, the reddening-corrected H γ intensity has the expected value of approximately 47% that of H β after correcting for reddening using the O300 H α intensity. In these four cases, then, H α and H γ would yield similar reddenings. Second, our ultimate aim is to calculate electron temperatures and oxygen abundances from these line intensities. If we measured the intensity of [O III] $\lambda 4363$ relative to H γ and [O III] $\lambda \lambda 4959, 5007$ relative to H β , and assumed $I(\text{H}\gamma)/I(\text{H}\beta) = 0.47$, we would obtain final intensities for the [O III] lines that would be statistically indistinguishable from those obtained by correcting for reddening using the H γ intensity. Applying a negative reddening correction does affect the oxygen abundance we derive by reducing the [O II] $\lambda 3727$ intensity, but this effect has less impact on the oxygen abundance than the uncertainty in the electron temperature since there is so little oxygen in the form of O $^+$. Third, forcing $I(\text{H}\gamma)/I(\text{H}\beta) = 0.47$ via a reddening correction, even if negative, accounts for any errors in the sensitivity calibration that might otherwise systematically affect the [O III] lines and the subsequent oxygen abundances. Fourth, on average, our H α - and H γ -based reddenings agree. The mean H α -based reddening for all objects

Table 4. Oxygen Abundances in M32

Object	T _e (K)	12+log(O/H) no ICF (dex)	12+log(O/H) KB94 ICF ^a (dex, adopted)
PN8	13000 ± 1400	8.36 ± 0.14	8.38 ± 0.14
PN11	< 25300	> 7.25	> 7.31
PN2	< 15700	> 8.17	> 8.27
PN7	< 13400	> 8.08	> 8.10
PN25	< 18600	> 8.02	> 8.08
PN24	18200 ± 2500	8.07 ± 0.13	8.13 ± 0.13
PN6	12700 ± 2500	8.46 ± 0.27	8.50 ± 0.27
PN5	11800 ± 1300	8.43 ± 0.16	8.46 ± 0.16
PN1	< 11500	> 8.39	> 8.41
PN4 ^b	< 12200	> 8.58	> 8.72
PN17 ^b	< 18400	> 7.84	> 7.92

^a Kingsburgh & Barlow 1994 ICF^b PN4 and PN17 are background objects in the disk of M31 (Ford & Jenner 1975).

(both M31 and M32) is $E(B - V) = 0.18 \pm 0.04$ mag, while the mean H γ -based reddening for all of the planetary nebulae in the bulge of M31 is $E(B - V) = 0.18 \pm 0.08$ mag, if negative reddening values are included, or $E(B - V) = 0.25 \pm 0.06$ mag, if negative reddening values are set to zero (the uncertainties are the standard errors in the means). Thus, the reddenings computed from H α and H γ are similar. For comparison, the foreground reddening to M31 is $E(B - V) = 0.093 \pm 0.009$ mag (mean of McClure & Racine 1969, van den Bergh 1969, and Burstein & Heiles 1984). It is not surprising that the mean reddening for the planetary nebulae is 0.10 mag greater than the foreground value, for planetary nebulae suffer additional reddening due to internal dust and dust within M31 and M32. Consequently, we have chosen to correct for “reddening” even when $E(B - V)$ is negative.

4. Oxygen abundances

Tables 4 and 5 present the electron temperatures and the oxygen abundances for the planetary nebulae in M32 and in the bulge of M31, respectively. We only observed two ionization stages of oxygen, O⁺ and O⁺⁺. We accounted for unseen stages in our oxygen abundance calculations using the ionization correction factors (ICF) computed according to the prescription of Kingsburgh & Barlow (1994), which employs the line intensities of He II $\lambda 4686$ and He I $\lambda 5876$ to correct for unseen ionization stages of oxygen. Further details may be found in Stasińska et al. (1998). Tables 4 and 5 present two oxygen abundance calculations. The abundances in column 3 are simply the sum of the O⁺ and O⁺⁺ ionic abundances. The abundances in column 4 are those from column 3 corrected for the ICF. The ICF is normally small because He II $\lambda 4686$ is weak.

Table 5. Oxygen Abundances in M31

Object	T _e (K)	12+log(O/H) no ICF (dex)	12+log(O/H) KB94 ICF ^a (dex, adopted)
PN172	13100 ± 1100	8.44 ± 0.10	8.46 ± 0.10
PN31	10700 ± 780	8.80 ± 0.10	8.80 ± 0.10
PN80	< 9500	> 8.91	> 8.91
PN30	< 9300	> 9.00	> 9.00
PN29	< 9800	> 8.91	> 8.91
PN28	< 8600	> 9.11	> 9.11
PN23	< 13200	> 8.30	> 8.30
PN12	13100 ± 2000	8.44 ± 0.18	8.51 ± 0.18
PN10	< 13600	> 8.22	> 8.24
PN1	< 10100	> 8.79	> 8.79
PN3	< 9400	> 8.96	> 8.96
PN38	< 10500	> 8.58	> 8.58
PN36	14600 ± 1600	8.12 ± 0.12	8.15 ± 0.12
PN53	9600 ± 870	8.91 ± 0.14	8.92 ± 0.14
PN52	< 11300	> 8.53	> 8.64
PN42	12400 ± 750	8.57 ± 0.08	8.59 ± 0.08
PN45	15100 ± 940	8.16 ± 0.07	8.17 ± 0.07
PN43	< 10200	> 8.71	> 8.72
PN48	9500 ± 640	8.95 ± 0.11	8.96 ± 0.11
PN95	< 9300	> 8.66	> 8.66
PN47	9600 ± 1200	8.77 ± 0.20	8.78 ± 0.20
PN408	< 13000	> 8.52	> 8.52
PN93	< 10500	> 8.79	> 8.80
PN92	11800 ± 1100	8.56 ± 0.12	8.57 ± 0.12
PN97	9400 ± 1000	8.87 ± 0.18	8.88 ± 0.18
PN91	12700 ± 1400	8.38 ± 0.13	8.38 ± 0.13
PN387	10600 ± 810	8.71 ± 0.12	8.74 ± 0.12
PN380	13900 ± 1100	8.38 ± 0.09	8.39 ± 0.09

^a Kingsburgh & Barlow 1994 ICF

The oxygen abundances in column 4 will be adopted in future work.

In calculating the oxygen abundances, we assumed an electron density of 4000 cm⁻³ in all cases. With electron densities of 1 cm⁻³ and 2 10⁴ cm⁻³, the oxygen abundance changes by a maximum of -0.02 dex and +0.07 dex, respectively, for the planetary nebulae in M31, and by a maximum of -0.03 dex and +0.11 dex, respectively, for the planetary nebulae in M32.

In instances where only upper limits to intensities were available, we adopted the following approach. When we had upper limits for the intensities of the helium lines these limits were used to calculate the ICF. If we did not observe He I $\lambda 5876$ (because it was outside our spectral window), we made no correction for unseen stages of oxygen regardless of the intensity of He II $\lambda 4686$. (Only in two cases, PN29 and PN30 in M31, did we detect He II $\lambda 4686$ when He I $\lambda 5876$ was outside our spectral window.) When we only had an upper limit to [O III] $\lambda 4363$, we used this to derive an upper limit to the electron temperature, and this

temperature limit was then used to derive a lower limit to the oxygen abundance. In these instances, we did not compute an error for either the electron temperature or the oxygen abundance, and have indicated the results listed in Tables 4 and 5 as limits. When we had an upper limit for $[\text{O II}]\lambda 3727$, we adopted this limiting intensity for the line. In this case, the O^+ ionic abundance is over-estimated, but its contribution to the total oxygen abundance was normally small.

Our uncertainties for the electron temperatures and oxygen abundances reflect the uncertainties in the $[\text{O III}]$ line intensities alone. As noted earlier, reddening introduces a further uncertainty through its effect upon $[\text{O II}]\lambda 3727$, but this has less influence upon the oxygen abundance than the uncertainty in the electron temperature. The electron temperature uncertainty that we quote is simply the temperature range permitted by the (1σ) limiting values of the $[\text{O III}]$ line intensities. Similarly, our oxygen abundance uncertainties are derived from the abundances calculated using the extreme values of the electron temperature.

5. Discussion

In Tables 4 and 5, we derive oxygen abundances for approximately half of the planetary nebulae we observed. For the rest, we derive lower limits. Many of the oxygen abundance limits, however, are very useful. Six of the fourteen temperature limits in Table 5 are below 10^4 K, and one is even below 9000 K. If we separate the planetary nebulae in Table 5 on the basis of whether they have temperatures or temperature limits, the mean oxygen abundances of the two sets differ at the 92% confidence level, with the set of objects with temperature limits having a higher mean oxygen abundance by at least 0.11 dex. Table 5 shows clearly that we are able to measure oxygen abundances up to approximately the solar value ($12 + \log(\text{O}/\text{H}) = 8.93$ dex; Anders & Grevesse 1989). Since the Loral3 CCD has only modest sensitivity at $[\text{O III}]\lambda 4363$, the quantum efficiency being about 22%, these results are by no means the limit of what is possible with 4m-class telescopes.

In several companion papers, we shall exploit the spectroscopic observations of planetary nebulae in M32 and in the bulge of M31 in several ways. First, we intend to study the evolution of the planetary nebulae in these galaxies relative to those in the Milky Way and the Magellanic Clouds. We also intend to investigate the chemical evolution of M32 and the bulges of M31 and the Milky Way individually as well as the chemical evolution of DHGs as a class.

Acknowledgements. We would like to thank George Jacoby for making several very helpful comments concerning a preliminary version of this paper, and for making further helpful suggestions as referee. MGR would like to thank the Natural Sciences and Engineering Research Council of Canada and Marshall McCall for their financial support while this research was

being done. MGR also thanks the Physics and Astronomy Department at York University for its hospitality and computing facilities while this work was being finished. MLM thanks the Natural Sciences and Engineering Research Council of Canada for its continuing support.

References

- Aller, L. H. 1987, *Physics of Thermal Gaseous Nebulae* (Dordrecht: D. Reidel Publishing Co.)
- Anders, E., & Grevesse, N. 1989, *Geochimica et Cosmochimica Acta*, 53, 197
- Anderson, E. 1987, *Reduction of Long-Slit Spectroscopic Data Using IRAF*, IRAF User Handbook, Vol 2B (Tucson: National Optical Astronomy Observatory)
- Bender, R., Burstein, D., & Faber, S. M. 1992, *ApJ*, 399, 462
- Bender, R., Burstein, D., & Faber, S. M. 1993, *ApJ*, 411, 153
- Brocato, E., Matteucci, F., Mazzitelli, I., & Tornambè, A. 1990, *ApJ*, 349, 458
- Burstein, D., & Heiles, C. 1984, *ApJS*, 54, 33
- Ciardullo, R., Jacoby, G. H., Ford, H. C., & Neill, J. D. 1989, *ApJ*, 339, 53
- Ford, H. C., & Jenner, D. C. 1975, *ApJ*, 202, 365
- Ford, H. C., Jacoby, G. H., & Jenner, D. C. 1978, *ApJ*, 223, 94
- Forestini, M., & Charbonnel, C. 1997, *A&AS*, 123, 241
- Henry, R. B. C. 1989, *MNRAS*, 241, 453
- Iben, I. Jr., & Renzini, A. 1983, *ARA&A*, 21, 271
- Kingsburgh, R. L., & Barlow, M. J. 1994, *MNRAS*, 271, 257
- Kormendy, J. 1985, *ApJ*, 295, 73
- Le Fèvre, O., Crampton, D., Felenbok, P., & Monnet, G. 1994, *A&A*, 282, 325
- Massey, P., Valdes, F., & Barnes, J. 1992, *A User's Guide to Reducing Spectra with IRAF*, IRAF User Guide, Vol 2B (Tucson: National Optical Astronomy Observatory)
- McCall, M. L. 1984, *MNRAS*, 208, 253
- McCall, M. L., Rybski, P. M., & Shields, G. A. 1985, *ApJS*, 57, 1
- McClure, R. D., & Racine, R. 1969, *AJ*, 74, 1000
- Osterbrock, D. E. 1989, *Astrophysics of Gaseous Nebulae and Active Galactic Nuclei* (Mill Valley: University Science Books)
- Perinotto, M. 1991, *ApJS*, 76, 687
- Richer, M. G. 1993, *ApJ*, 415, 240
- Schild, R. E. 1977, *AJ*, 82, 337
- Stasińska, G., Richer, M. G., & McCall, M. L. 1998, *A&A*, 366, 667
- van den Bergh, S. 1969, *ApJS*, 19, 145
- Wheeler, J. C., Sneden, C., & Truran, J. W. Jr. 1989, *ARA&A*, 27, 279

Table 6. Line Intensities for PNe in M32

Wavelength	PN5	O300	B600	U900	PN1	O300	B600	U900
3727 ^a	29.0 ± 8.3			29.0 ± 8.3	83 ± 13			83 ± 13
3868.76	94.0 ± 9.9		100 ± 19	94.0 ± 9.9	110 ± 12		78 ± 13	110 ± 12
3967.47	48.6 ± 9.3			48.6 ± 9.3	49 ± 11			49 ± 11
4101.737	29.8 ± 5.8			29.8 ± 5.8	33.3 ± 5.8		27.1 ± 8.5	33.3 ± 5.8
4340.468	47.0 ± 6.6		±13	47.0 ± 6.6	47.0 ± 6.8	48.6 ± 8.8	42.2 ± 5.9	47.0 ± 6.8
4363.21	14.0 ± 4.4		±13	14.0 ± 4.4	±10	±16	±9	±10
4685.682	±17	±17	±14	10.0 ± 3.3	10.8 ± 3.7	±7	10.8 ± 3.7	±11
4861.332	100.0 ± 5.4	100.0 ± 5.4	100.0 ± 8.8		100.0 ± 4.0	100.0 ± 4.0	100.0 ± 4.8	
4958.92	431.7 ± 5.0	431.7 ± 5.0	448 ± 26		337.8 ± 4.6	337.8 ± 4.6	349 ± 11	
5006.85	1291.8 ± 6.9	1291.8 ± 6.9	1343 ± 71		994.1 ± 6.7	994.1 ± 6.7	1052 ± 29	
5875.666	16.0 ± 4.0	16.0 ± 4.0	18.8 ± 4.9		21.2 ± 1.6	21.2 ± 1.6	22.3 ± 2.6	
6300.32	±6	±6			±2	±2		
6312.06	10.4 ± 3.6	10.4 ± 3.6			±2	±2		
6363.81	±6	±6			±2	±2		
6548.06	29.6 ± 3.2	29.6 ± 3.2			76.7 ± 2.1	76.7 ± 2.1		
6562.817	285.0 ± 4.0	285.0 ± 4.0			285.0 ± 2.7	285.0 ± 2.7		
6583.39	102.7 ± 3.5	102.7 ± 3.5			230.6 ± 2.5	230.6 ± 2.5		
6716.42					10.21 ± 0.92	10.21 ± 0.92		
6730.72					17.08 ± 0.99	17.08 ± 0.99		
7065.277	13.0 ± 4.1	13.0 ± 4.1			3.5 ± 1.0	3.5 ± 1.0		
7135.8	30.2 ± 4.8	30.2 ± 4.8			18.0 ± 1.3	18.0 ± 1.3		
7325	10.4 ± 3.3	10.4 ± 3.3			3.11 ± 0.56	3.11 ± 0.56		
9069	12.7 ± 3.1	12.7 ± 3.1						
$E(B - V)$	0.01 ± 0.01				0.11 ± 0.01			
Wavelength	PN4, M31	O300	B600	U900	PN17, M31	O300	B600	U900
3727 ^a	106 ± 36			106 ± 36	±64			±64
3868.76	169 ± 32			169 ± 32	79 ± 22			79 ± 22
3967.47	53 ± 15			53 ± 15				
4101.737	50 ± 17			50 ± 17	±34			±34
4340.468	47 ± 13			47 ± 13	41 ± 13			41 ± 13
4363.21	±22			±22	±29			±29
4685.682	51 ± 11	51 ± 11	37 ± 10	55 ± 14	±22	±26	±25	±22
4861.332	100 ± 11	100 ± 11	100 ± 12		100 ± 12	100 ± 12	100 ± 14	100 ± 10
4958.92	637 ± 10	637 ± 10	703 ± 50		337 ± 12	337 ± 12	384 ± 38	253 ± 18
5006.85	1916 ± 14	1916 ± 14	2137 ± 149		993 ± 16	993 ± 16	1176 ± 110	807 ± 48
5875.666	10.9 ± 4.7	±4	10.9 ± 4.7		13.0 ± 3.4	13.0 ± 3.4	19.3 ± 4.9	
6300.32	±6	±6			±4	±4		
6312.06	±6	±6			±4	±4		
6363.81	±6	±6			±4	±4		
6548.06	15.6 ± 4.0	15.6 ± 4.0			26.3 ± 2.4	26.3 ± 2.4	29.6 ± 5.3	
6562.817	285.0 ± 5.7	285.0 ± 5.7			285.0 ± 4.1	285.0 ± 4.1	349 ± 33	
6583.39	45.4 ± 4.5	45.4 ± 4.5			77.3 ± 2.7	77.3 ± 2.7	91.7 ± 9.8	
7135.8	21.8 ± 3.1	21.8 ± 3.1			22.5 ± 4.1		22.5 ± 4.1	
7325	14.4 ± 5.4	14.4 ± 5.4			14.2 ± 1.9	14.2 ± 1.9		
$E(B - V)$	0.15 ± 0.02				0.57 ± 0.01			

^a “3727” denotes the sum of [O II] $\lambda\lambda$ 3726,3729

Table 7. Line Intensities for PNe in M32 (continued)

Wavelength	PN8	O300	B600	U900	PN2	O300	B600	U900
3726.05	38.1 ± 9.0			38.1 ± 9.0	±35			±35
3728.8	41.9 ± 9.1			41.9 ± 9.1	85 ± 22			85 ± 22
3868.76	121 ± 10			121 ± 10	98 ± 17			98 ± 17
3967.47	62 ± 13			62 ± 13	60 ± 17			60 ± 17
4101.737	24.1 ± 7.6			24.1 ± 7.6	±21			±21
4340.468	59.7 ± 6.8		42.4 ± 6.0	59.7 ± 6.8	73 ± 17			73 ± 17
4363.21	19.1 ± 5.3		13.4 ± 4.7	19.1 ± 5.3	±31			±31
4685.682	±11	5.3 ± 2.5	±8	±11	22.8 ± 7.7	16.5 ± 7.9	44 ± 11	22.8 ± 7.7
4861.332	100.0 ± 4.6	100.0 ± 4.6	100.0 ± 6.0	100.0 ± 7.1	100 ± 10	100 ± 10	100 ± 13	100 ± 11
4958.92	462.5 ± 7.6	462.5 ± 7.6	458 ± 17	434 ± 18	508.7 ± 7.3	508.7 ± 7.3	723 ± 61	520 ± 36
5006.85	1386 ± 11	1386 ± 11	1364 ± 48	1334 ± 52	1461.1 ± 9.5	1461.1 ± 9.5	2109 ± 172	1602 ± 100
5875.666	16.6 ± 1.1	16.6 ± 1.1	18.2 ± 2.2		8.3 ± 2.5	8.3 ± 2.5	16.4 ± 5.6	
6300.32	5.8 ± 1.4	5.8 ± 1.4			8.6 ± 2.6	8.6 ± 2.6		
6312.06	3.2 ± 1.3	3.2 ± 1.3			±3	±3		
6363.81	±2	±2			±3	±3		
6548.06	57.0 ± 1.2	57.0 ± 1.2	51.0 ± 3.7		30.9 ± 2.0	30.9 ± 2.0	50.6 ± 8.3	
6562.817	285.0 ± 1.9	285.0 ± 1.9	275.4 ± 10		285.0 ± 2.7	285.0 ± 2.7	414 ± 35	
6583.39	168.2 ± 1.5	168.2 ± 1.5	158.2 ± 6.7		102.4 ± 2.3	102.4 ± 2.3	159 ± 15	
6716.42	11.2 ± 1.1	11.2 ± 1.1	9.8 ± 1.9		9.0 ± 1.8	9.0 ± 1.8	±13	
6730.72	17.1 ± 1.2	17.1 ± 1.2			14.0 ± 1.9	14.0 ± 1.9		
7065.277	5.75 ± 0.71	5.75 ± 0.71						
7135.8	17.66 ± 0.84	17.66 ± 0.84	15.3 ± 2.7		19.7 ± 2.0	19.7 ± 2.0	21.2 ± 6.0	
7325	2.36 ± 0.57	2.36 ± 0.57						
9069	13.2 ± 1.2	13.2 ± 1.2			20.1 ± 3.3	20.1 ± 3.3		
9531.8	34.0 ± 3.7	34.0 ± 3.7			32.2 ± 4.7	32.2 ± 4.7		
$E(B - V)$	0.20 ± 0.01				0.06 ± 0.01			
Wavelength	PN11	O300	B600	U900	PN7	O300	B600	U900
3726.05	123 ± 20			123 ± 20	25.2 ± 8.2			25.2 ± 8.2
3728.8	119 ± 20			119 ± 20	±11			±11
3868.76	21.0 ± 8.3			21.0 ± 8.3	48 ± 10		49 ± 17	48 ± 10
3967.47	16.5 ± 6.8			16.5 ± 6.8	21.3 ± 5.4			21.3 ± 5.4
4101.737	16.9 ± 8.3			16.9 ± 8.3	24.8 ± 8.7			24.8 ± 8.7
4340.468	21.1 ± 9.4		±47	21.1 ± 9.4	47.0 ± 8.4		38.5 ± 6.8	47.0 ± 8.4
4363.21	±14			±14	±12		±9	±12
4685.682	±16	±15	±21	±16	11.9 ± 4.8	11.9 ± 4.8	±9	
4861.332	100.0 ± 9.2	100.0 ± 9.2	100 ± 16	100.0 ± 9.5	100.0 ± 5.5	100.0 ± 5.5	100.0 ± 5.9	
4958.92	91.4 ± 6.5	91.4 ± 6.5	106 ± 14	94.6 ± 9.2	274.5 ± 4.3	274.5 ± 4.3	282 ± 11	
5006.85	298.4 ± 8.7	298.4 ± 8.7	320 ± 34	263 ± 17	805.8 ± 5.9	805.8 ± 5.9	863 ± 31	
5875.666	17.1 ± 3.0	17.1 ± 3.0	15.2 ± 6.9		14.0 ± 1.4	14.0 ± 1.4	12.5 ± 2.0	
6300.32	±4	±4						
6312.06	±4	±4						
6363.81	±4	±4						
6548.06	60.3 ± 2.5	60.3 ± 2.5	75.5 ± 12.2		5.7 ± 1.2	5.7 ± 1.2		
6562.817	285.0 ± 5.1	285.0 ± 5.1	315 ± 33		285.0 ± 2.1	285.0 ± 2.1		
6583.39	178.7 ± 3.7	178.7 ± 3.7	199 ± 23		12.3 ± 1.3	12.3 ± 1.3		
6716.42	12.0 ± 2.0	12.0 ± 2.0	±13		±3	±3		
6730.72	16.3 ± 2.1	16.3 ± 2.1			±3	±3		
7065.277					6.4 ± 1.1	6.4 ± 1.1		
7135.8	8.5 ± 2.2	8.5 ± 2.2			5.5 ± 1.0	5.5 ± 1.0		
7325	5.7 ± 2.0	5.7 ± 2.0						
9069	9.3 ± 3.1	9.3 ± 3.1						
$E(B - V)$	0.05 ± 0.02				0.03 ± 0.01			

Table 8. Line Intensities for PNe in M32 (continued)

Wavelength	H II #1	O300	B600	U900	PN24	O300	B600	U900
3726.05	98 ± 33			98 ± 33	73 ± 15			73 ± 15
3727 ^a			148 ± 40					
3728.8	58 ± 27			58 ± 27	48 ± 13			48 ± 13
3868.76	26 ± 14			26 ± 14	134 ± 20		135 ± 36	134 ± 20
3967.47					54 ± 15			54 ± 15
4101.737	±21			±21	±30			±30
4340.468	47 ± 16		±13	47 ± 16	67 ± 13		46 ± 16	67 ± 13
4363.21	±23		±13	±23	47 ± 12			47 ± 12
4685.682	±17	±8	±17		39 ± 12	±34	32 ± 13	39 ± 12
4861.332	100.0 ± 6.5	100.0 ± 6.5	100 ± 11		100 ± 19	100 ± 19	100 ± 21	100 ± 14
4958.92	63.0 ± 5.8	63.0 ± 5.8	73.1 ± 7.5		572 ± 23	572 ± 23	541 ± 71	465 ± 41
5006.85	205.5 ± 7.5	205.5 ± 7.5	215 ± 15		1654 ± 30	1654 ± 30	1585 ± 202	
5875.666	11.5 ± 1.8	11.5 ± 1.8			22 ± 10	64 ± 14	22 ± 10	
6300.32	±4	±4			±27	±27		
6312.06	±4	±4			±27	±27		
6363.81	±4	±4			±27	±27		
6548.06	28.3 ± 2.3	28.3 ± 2.3			94.7 ± 9.7	94.7 ± 9.7	63.0 ± 15.1	
6562.817	285.0 ± 5.5	285.0 ± 5.5			285 ± 11	285 ± 11	241 ± 34	
6583.39	23.6 ± 2.0	23.6 ± 2.0			268 ± 11	268 ± 11	214 ± 31	
6716.42					9.5 ± 2.5	9.5 ± 2.5		
6730.72					11.4 ± 2.7	11.4 ± 2.7		
7135.8					17.3 ± 4.0	17.3 ± 4.0		
9069					17.5 ± 3.8	17.5 ± 3.8		
$E(B - V)$	0.29 ± 0.02				0.15 ± 0.03			
Wavelength	PN25	O300	B600	U900	PN6	O300	B600	U900
3727 ^a	±65			±65	21.3 ± 15			21.3 ± 15.2
3868.76	152 ± 38			152 ± 38	127 ± 31		127 ± 29	127 ± 31
4101.737	38 ± 19			38 ± 19	16.2 ± 9.2			16.2 ± 9.2
4340.468	±48	180 ± 44		±48	47 ± 15		±22	47 ± 15
4363.21	±48	84 ± 36			23 ± 11		±22	23 ± 11
4685.682	±38	±73		±38	32 ± 12	±36	34 ± 15	32 ± 12
4861.332	100 ± 43	100 ± 43	±118	100 ± 27	100 ± 20	100 ± 20	100 ± 17	
4958.92	595 ± 49	595 ± 49	1115 ± 547		598 ± 23	598 ± 23	438 ± 50	
5006.85	1600 ± 66	1600 ± 66	3338 ± 1626		1731 ± 30	1731 ± 30	1314 ± 133	
5875.666	35.9 ± 4.1	35.9 ± 4.1	±102		29.6 ± 6.5	±26	29.6 ± 6.5	
6300.32	±26	±26			±12	±12		
6312.06	±26	±26			±12	±12		
6363.81	±26	±26			±12	±12		
6548.06	±57	±57	±93		±15	±15		
6562.817	285 ± 32	285 ± 32	470 ± 236		285 ± 10	285 ± 10		
6583.39	159 ± 28	159 ± 28	473 ± 238		42.0 ± 7.3	42.0 ± 7.3		
7135.8	±46	±46			±12	±12		
9069	21.8 ± 5.9	21.8 ± 5.9						
$E(B - V)$	0.31 ± 0.10				0.17 ± 0.03			

^a “3727” denotes the sum of [O II]λλ3726,3729

Table 9. Line Intensities for PNe in the bulge of M31

Wavelength	PN172	PN31	PN80	PN30	PN29	PN28	PN23
3727	± 29	± 30	41.3 ± 8.7	109 ± 19	± 29	± 43	± 25
3868.76	138 ± 16	181 ± 13	90.9 ± 8.6	108 ± 10	104 ± 15	95 ± 16	137 ± 21
3967.47	56 ± 10	59 ± 11	38.7 ± 8.4	44 ± 10	42 ± 10	41 ± 11	52 ± 15
4101.737	27.5 ± 7.0	18.0 ± 4.7	32 ± 10	29.1 ± 5.6	25.9 ± 6.4	21.8 ± 9.0	25 ± 12
4340.468	47.0 ± 5.4	47.0 ± 4.5	47.0 ± 5.9	47.0 ± 6.3	47.0 ± 8.6	47.0 ± 7.9	47.0 ± 9.9
4363.21	25.8 ± 4.7	18.2 ± 3.6	± 10	± 10	± 14	± 8	± 19
4685.682	± 6	± 6	± 8	24.1 ± 4.0	21.6 ± 5.0	± 10	± 14
4861.332	100.0 ± 5.0	100.0 ± 4.4	100.0 ± 5.0	100.0 ± 4.9	100.0 ± 6.9	100.0 ± 7.8	100.0 ± 8.5
4958.92	613 ± 18	737 ± 21	605 ± 20	645 ± 21	691 ± 30	685 ± 32	459 ± 26
5006.85	1819 ± 49	2253 ± 59	1869 ± 60	2063 ± 63	2219 ± 91	2151 ± 96	1347 ± 75
5875.666	15.6 ± 2.3						
$E(B - V)$	0.41 ± 0.30	0.40 ± 0.25	-0.16 ± 0.33	0.16 ± 0.35	-0.03 ± 0.48	0.15 ± 0.44	0.74 ± 0.56
Wavelength	PN12	PN10	PN1	PN3	PN38	PN36	PN53
3727	± 86	± 25	± 40	± 11	18.9 ± 7.0	± 31	22.6 ± 6.2
3868.76	176 ± 30	70 ± 12	158 ± 18	64.6 ± 6.9	57.4 ± 8.1	130 ± 15	84.0 ± 7.4
3967.47	55 ± 16	33 ± 11	63 ± 12	22.5 ± 5.6	23.9 ± 6.8	103 ± 15	37.7 ± 6.6
4101.737	26 ± 11	± 19	31.0 ± 8.6	± 13	34.0 ± 6.8	29.4 ± 8.8	15.2 ± 2.9
4340.468	47.0 ± 9.9	47 ± 12	47.0 ± 8.7	47.0 ± 6.7	47.0 ± 5.9	47.0 ± 5.4	47.0 ± 4.5
4363.21	24.7 ± 8.0	± 18	± 12	± 12	± 9	20.7 ± 4.5	11.8 ± 3.4
4685.682	21.2 ± 7.7	± 15	± 15	± 11	± 8	± 7	± 5
4861.332	100.0 ± 8.6	100 ± 11	100 ± 10	100.0 ± 9.1	100.0 ± 6.1	100.0 ± 5.0	100.0 ± 4.1
4958.92	586 ± 38	396 ± 29	593 ± 36	672 ± 37	408 ± 16	382 ± 13	674 ± 18
5006.85	1734 ± 112	1183 ± 81	1825 ± 109	2153 ± 115	1256 ± 44	1136 ± 35	2062 ± 52
5875.666	10.6 ± 3.6	25.3 ± 7.1		59.3 ± 11.0		8.8 ± 1.6	38.2 ± 5.3
$E(B - V)$	0.88 ± 0.56	0.18 ± 0.68	0.49 ± 0.49	-0.55 ± 0.38	-0.09 ± 0.33	0.78 ± 0.30	-0.31 ± 0.25
Wavelength	PN52	PN42	PN45	PN43	PN48	PN95	PN47
3727	± 63	± 19	26.1 ± 7.7	± 14	± 10	19.7 ± 6.1	19.5 ± 7.5
3868.76	63 ± 12	122.2 ± 8.0	120.5 ± 7.8	56.7 ± 6.9	125.9 ± 5.6	60.7 ± 3.4	63.9 ± 5.0
3967.47	32 ± 10	32.9 ± 8.0	56.9 ± 6.3	30.2 ± 5.8	42.7 ± 5.8	28.5 ± 4.8	35.4 ± 6.6
4101.737	43 ± 14	16.8 ± 4.1	25.2 ± 5.4	14.8 ± 4.3	22.1 ± 2.9	23.4 ± 3.6	21.6 ± 4.5
4340.468	47.0 ± 9.9	47.0 ± 4.3	47.0 ± 3.6	47.0 ± 6.5	47.0 ± 3.3	47.0 ± 3.4	47.0 ± 4.4
4363.21	± 13	25.9 ± 3.7	27.2 ± 3.2	± 11	11.7 ± 2.6	± 5	8.1 ± 3.2
4685.682	22.2 ± 6.7	± 6	± 4	± 7	4.0 ± 1.9	± 3	± 4
4861.332	100.0 ± 8.2	100.0 ± 4.7	100.0 ± 3.4	100.0 ± 4.9	100.0 ± 3.3	100.0 ± 2.4	100.0 ± 3.6
4958.92	464 ± 27	694 ± 19	462 ± 10	521 ± 18	700 ± 14	331.1 ± 5.8	474 ± 10
5006.85	1364 ± 75	2111 ± 54	1381 ± 27	1576 ± 52	2160 ± 43	998 ± 15	1452 ± 28
5875.666	± 6	12.0 ± 1.8	15.9 ± 1.6	34.1 ± 6.7	36.1 ± 3.7	18.6 ± 1.5	20.9 ± 2.4
$E(B - V)$	0.63 ± 0.56	0.30 ± 0.24	0.44 ± 0.20	-0.72 ± 0.36	-0.25 ± 0.19	0.11 ± 0.19	0.09 ± 0.25
Wavelength	PN408	PN93	PN92	PN97	PN91	PN387	PN380
3727		39.1 ± 8.9	73 ± 14	± 17	± 30	126 ± 17	± 26
3868.76		84.2 ± 6.8	129 ± 13	79.5 ± 8.2	63.8 ± 9.9	111 ± 9.4	108 ± 10
3967.47		27.3 ± 5.4	44.8 ± 8.5	44.5 ± 4.3	29.5 ± 8.1	43.9 ± 6.9	51.8 ± 9.6
4101.737		21.9 ± 4.8	34.7 ± 7.9	21.7 ± 4.5	± 14	30.3 ± 6.2	28.8 ± 6.8
4340.468		47.0 ± 8.7	47.0 ± 5.0	51.6 ± 4.4	47.0 ± 6.0	47.0 ± 3.5	50.4 ± 5.7
4363.21		± 16	18.4 ± 4.1	9.3 ± 3.4	18.9 ± 4.8	12.3 ± 2.7	30.5 ± 5.1
4685.682		15.0 ± 3.8	± 6	± 4	± 8	15.3 ± 2.7	± 5
4861.332	100 ± 29	100.0 ± 5.4	100.0 ± 4.0	100.0 ± 3.2	100.0 ± 5.3	100.0 ± 4.0	100.0 ± 4.6
4958.92	491 ± 85	673 ± 24	565 ± 15	565 ± 13	482 ± 17	525 ± 15	614 ± 22
5006.85	1431 ± 242	2070 ± 72	1703 ± 42	1744 ± 35	1437 ± 44	1591 ± 36	1851 ± 48
5875.666		30.0 ± 6.0	17.2 ± 1.8	22.7 ± 2.4		16.1 ± 1.3	18.3 ± 1.5
6548.06				12.0 ± 2.1			4.4 ± 1.8
6562.817				285.0 ± 6.4			285.0 ± 7.3
6583.39				35.8 ± 2.5			16.9 ± 2.0
$E(B - V)$		-0.24 ± 0.49	0.51 ± 0.28	0.02 ± 0.02	0.26 ± 0.34	0.39 ± 0.20	0.20 ± 0.02

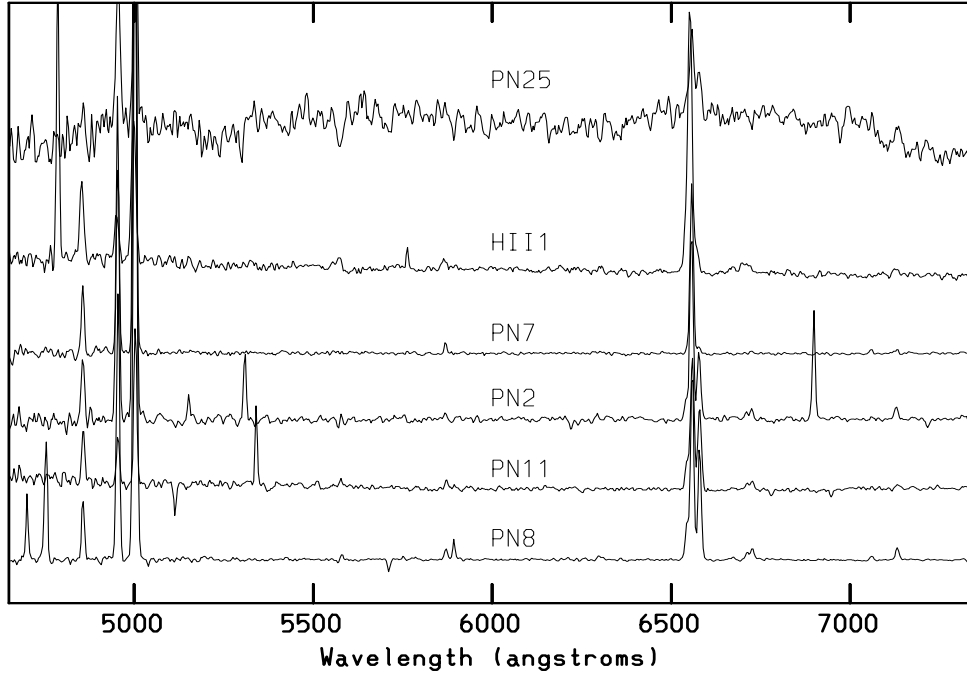


Fig. 1. The O300 spectra for PN8, PN11, PN2, PN7, H II 1, and PN25 in the M32 field. The spectra are displayed such that $H\beta$ spans the entire free intensity scale. Consequently, lines stronger than $H\beta$ overlap in adjacent spectra. We show only the spectral range blueward of 7350Å. In all of the spectra we present, cosmic rays were not removed unless they interfered with measuring line intensities, so many obviously remain. PN25 is very close to M32's nucleus, so the sky subtraction is poorer for this object. H II 1 is an H II region in the background disk of M31 (Ford & Jenner 1975).

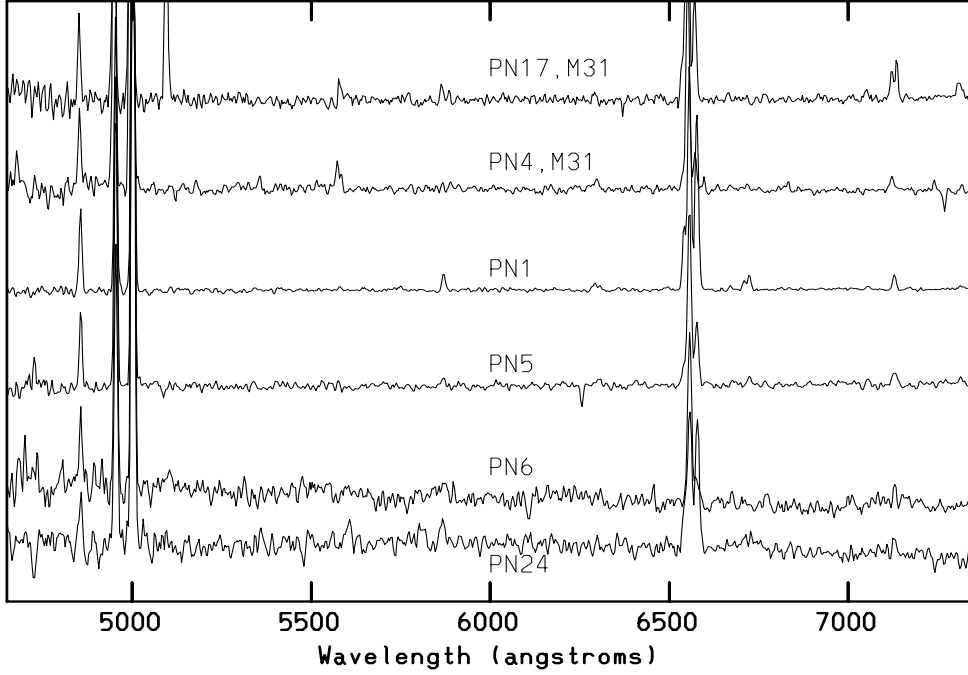


Fig. 2. The O300 spectra for PN24, PN6, PN5, PN1, PN4, and PN17 in the M32 field. The format is identical to Fig. 1. Like PN25, PN24 is also very close to M32's nucleus and suffers from somewhat poorer background subtraction. Note that PN4 and PN17 are background planetary nebulae in the disk of M31 (Ford & Jenner 1975).

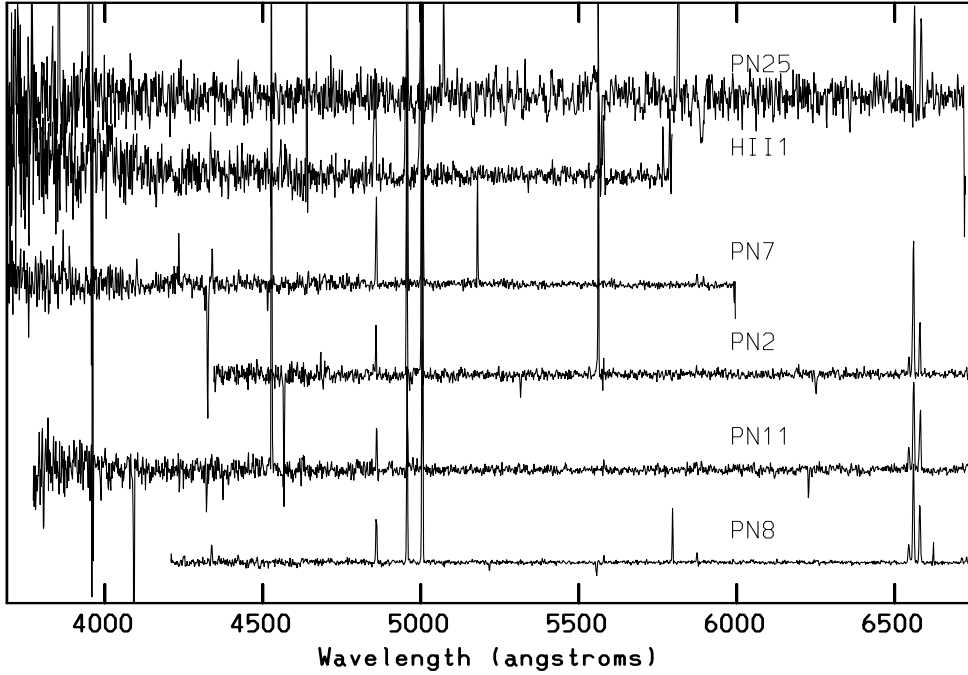


Fig. 3. The B600 spectra for PN8, PN11, PN2, PN7, HII 1, and PN25 in the M32 field. For PN8, PN11, and PN25, the scaling is such that H α , not H β , defines the free intensity range. The full useful wavelength range of the spectra, 3690Å to 6750Å, is shown. See Fig. 1 for comments on individual objects.

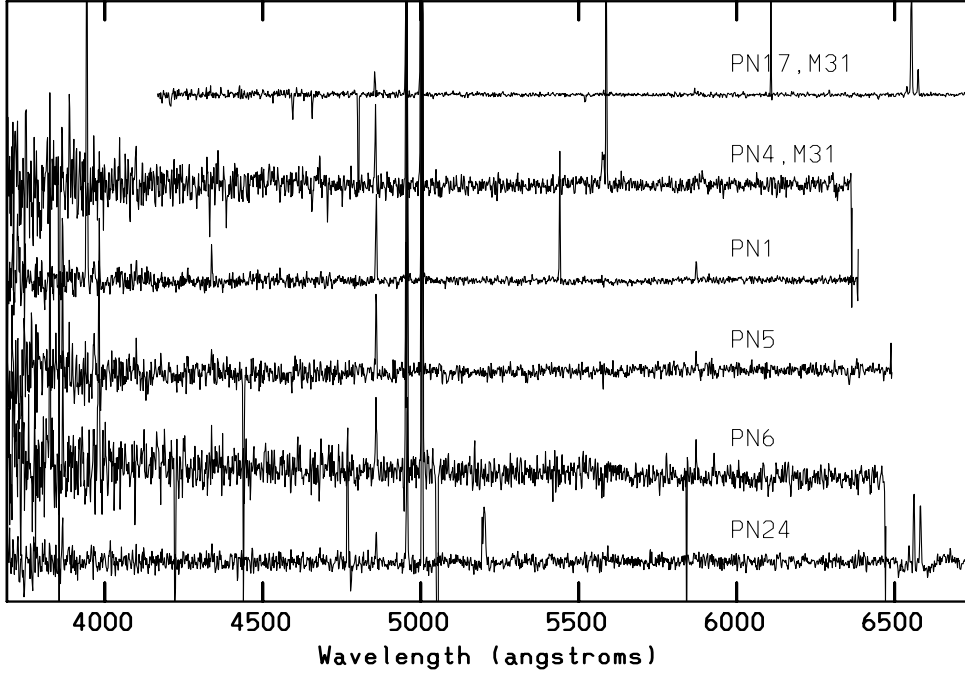


Fig. 4. The B600 spectra for PN24, PN6, PN5, PN1, PN4, and PN17 in the M32 field. For PN24 and PN17 (M31), $H\alpha$, and not $H\beta$, defines the free intensity range. The full useful wavelength range of the spectra, 3690Å to 6750Å, is shown. See Fig. 2 for comments on individual objects.

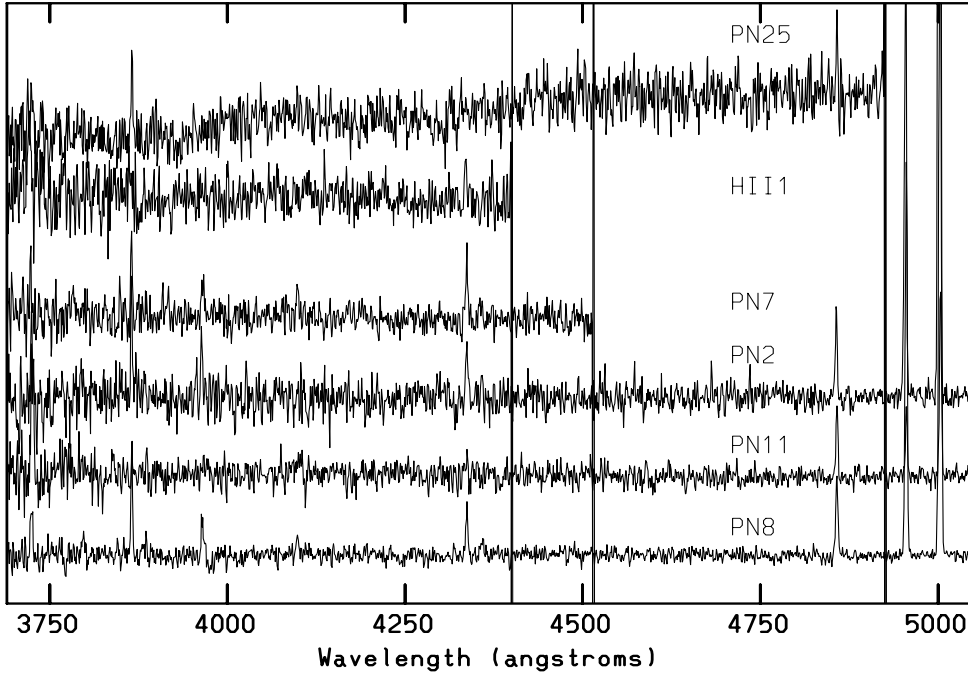


Fig. 5. The U900 spectra for PN8, PN11, PN2, PN7, HII 1, and PN25 in the M32 field. Only for PN11 and PN25 does $H\beta$ define the full intensity scale. For the other objects, the full intensity scale is defined by $H\gamma$. The full useful wavelength range, 3690Å to 5050Å, is displayed. See Fig. 1 for comments on individual objects.

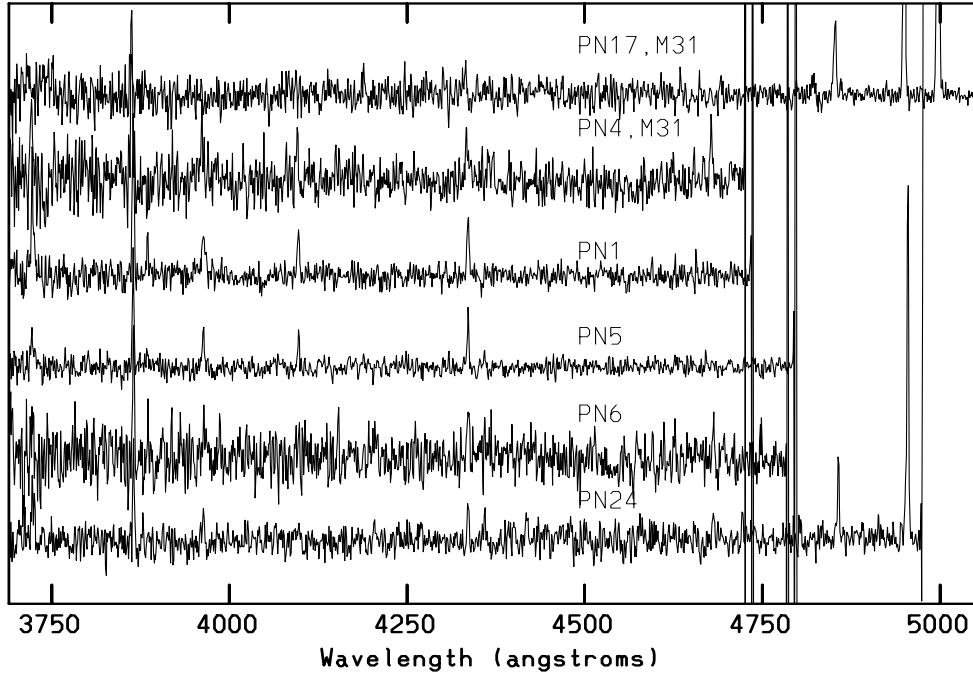


Fig. 6. The U900 spectra for PN24, PN6, PN5, PN1, PN4, and PN17 in the M32 field. $H\beta$ defines the full intensity scale for PN24 and PN17, but $H\gamma$ does so for the other objects. The full useful wavelength range, 3690Å to 5050Å, is displayed. See Fig. 2 for comments on individual objects.

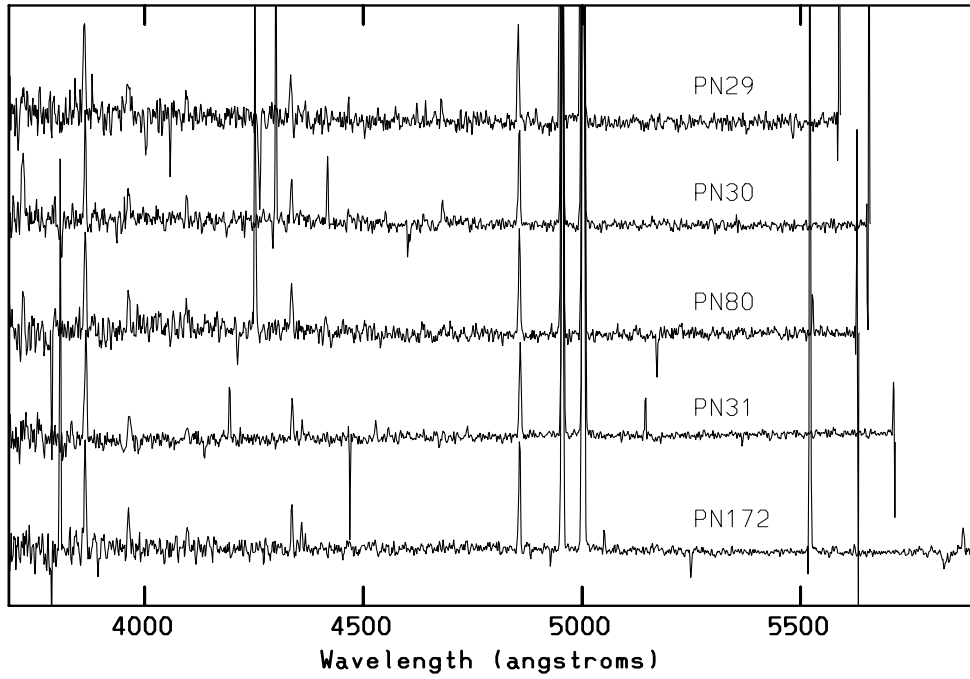


Fig. 7. The B600 spectra for PN172, PN31, PN80, PN30, and PN29 in the M31 bulge field. The intensity scaling is set so that $H\beta$ occupies the full free intensity scale in all cases, and the entire useful wavelength range is shown.

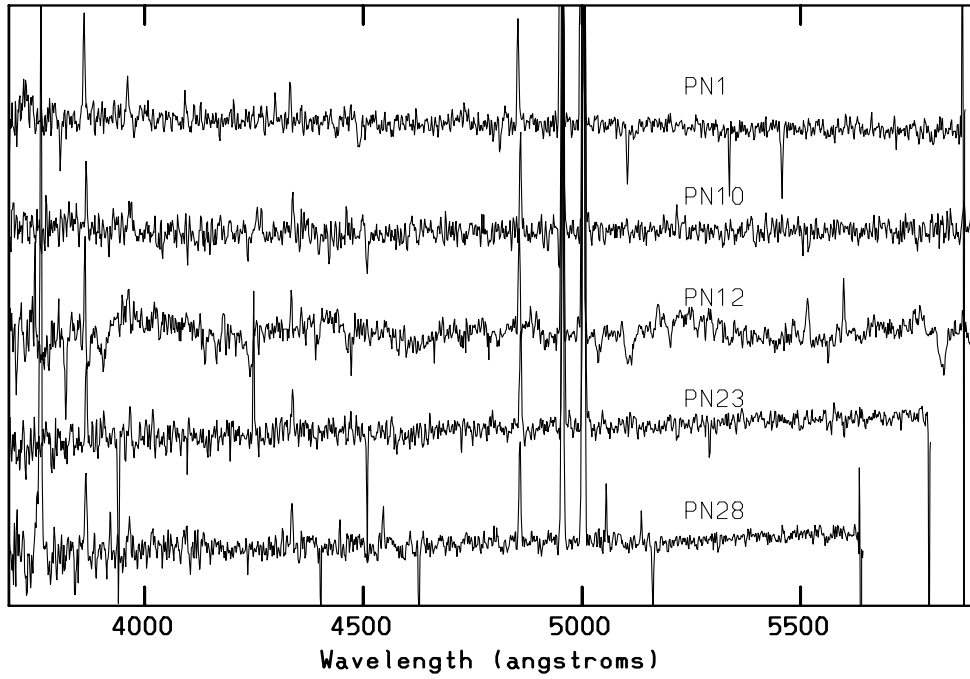


Fig. 8. The B600 spectra for PN28, PN23, PN12, PN10, and PN1 in the M31 bulge field. The intensity and wavelength scales are as in Fig. 7. Note that the background subtraction is poorer for PN12 than is normally the case.

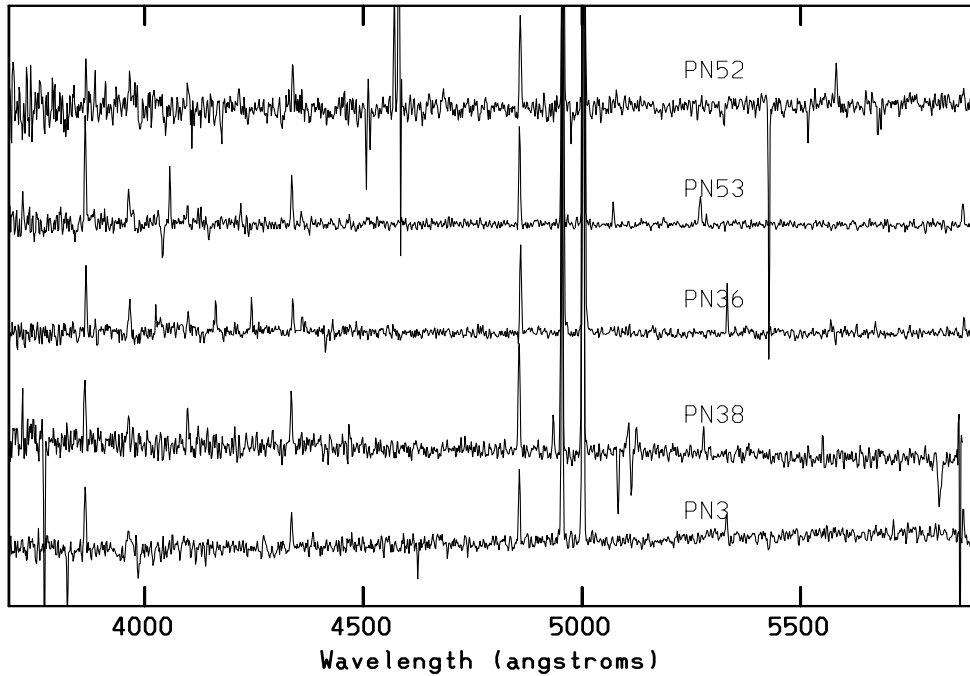


Fig. 9. The B600 spectra for PN3, PN38, PN36, PN53, and PN52 in the M31 bulge field. The intensity and wavelength scales are as in Fig. 7.

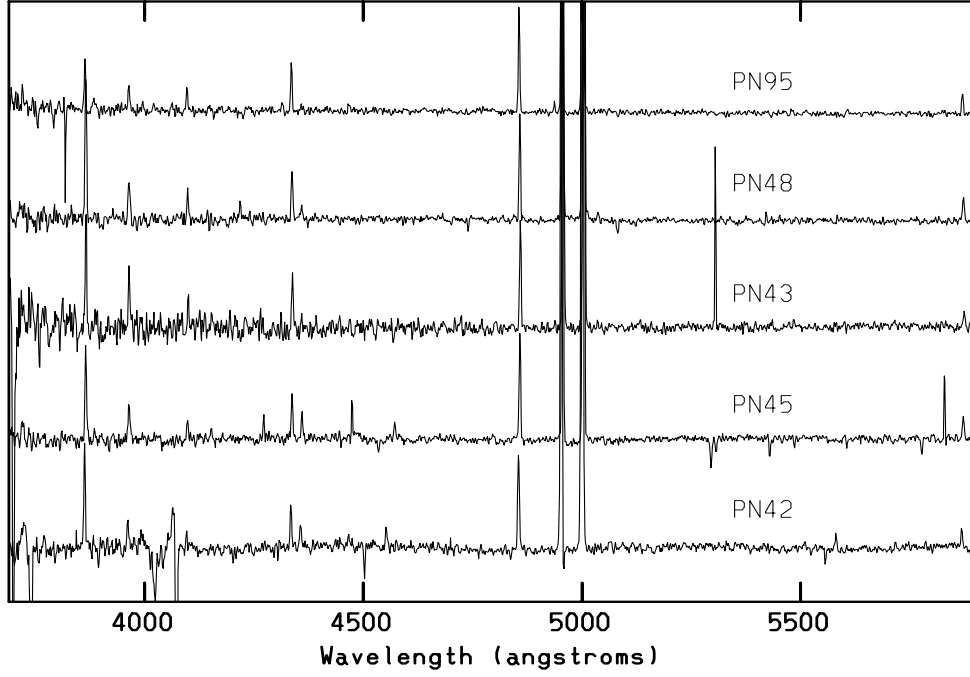


Fig. 10. The B600 spectra for PN42, PN45, PN43, PN48, and PN95 in the M31 bulge field. The intensity and wavelength scales are as in Fig. 7.

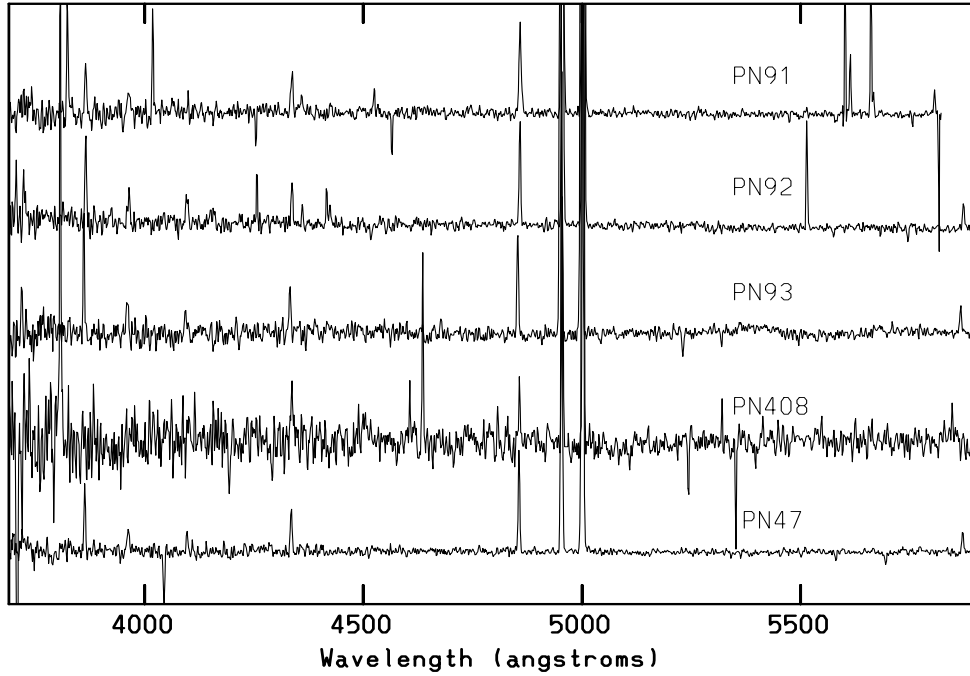


Fig. 11. The B600 spectra for PN47, PN408, PN93, PN92, and PN91 in the M31 bulge field. The intensity and wavelength scales are as in Fig. 7. Note that the signal-to-noise is poor for the very faint object PN408.

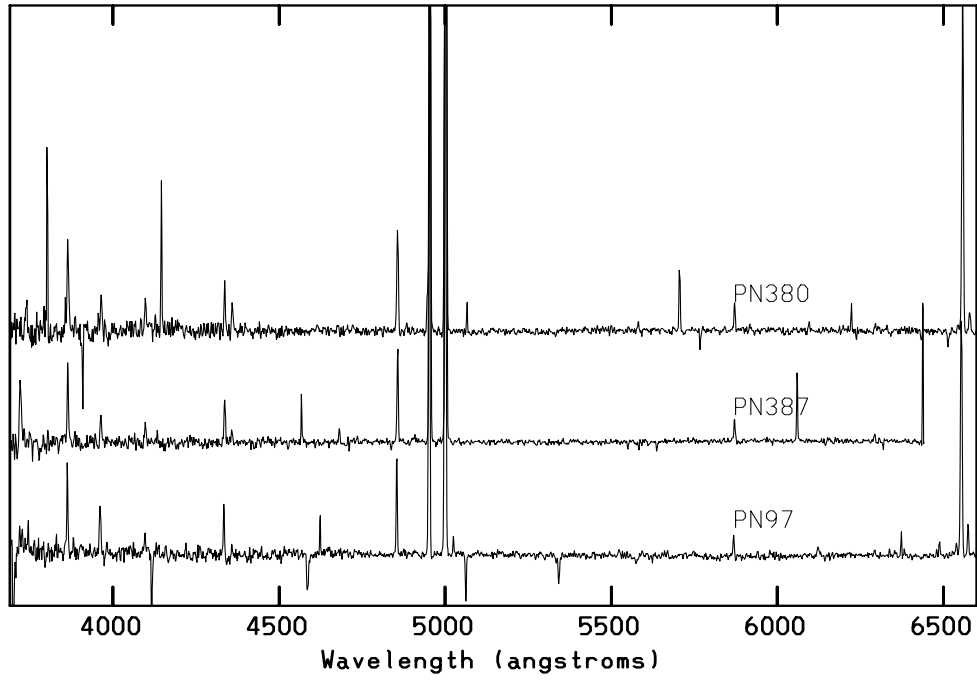


Fig. 12. The B600 spectra for PN97, PN387, and PN380 in the M31 bulge field. The intensity scaling is set so that $H\beta$ occupies the full free intensity scale in all cases, and the entire useful wavelength range is shown. For PN97 and PN380, though, the wavelength range extends to 6600Å.